ORIGINAL PAPER

A Lattice Spring Model for Coupled Fluid Flow and Deformation Problems in Geomechanics

GaoFeng Zhao · Nasser Khalili

Abstract   A lattice spring model is developed for coupled fluid flow and deformation problems. The model has an underlying structure consisting of particles connected by springs for the solid and fluid bubbles, connected by fluid pipelines for fluid flow. Formulations of the model to describe the coupled fluid flow and deformation behavior of a solid are derived. A few examples of consolidation problems are presented and compared with analytical solutions with good agreement being obtained, which means that the lattice model developed in this study can correctly simulate the coupled fluid flow and deformation response of a solid.

Keywords   Lattice spring model · Fluid flow · Saturated media

List of Symbols

Roman Alphabet

A_0	The total area of the interface between the fluid bubble and solid particle
A_c	The contact area between the solid particles
A^{ele}	The area of the triangle element
A^p	The cross-sectional area of the pipe
$\bar{A}$	The area of the model
$\mathbf{B}$	The strain interpolation matrix of the bond
c_f	The compressibility of the fluid
C_g	The compressibility of the solid grain
C_s	The compressibility of the skeleton

G. Zhao (✉) · N. Khalili
School of Civil and Environmental Engineering, The University of New South Wales, Sydney, NSW 2052, Australia
e-mail: gaofeng.zhao@unsw.edu.au

$\mathbf{C}_{global}$	The global matrix of pore pressure and particle force relationship
E	The Young's modulus
E_g	The elastic modulus of solid particle
E_s	The elastic modulus of porous material
$\mathbf{F}$	The vector of particle forces
$\mathbf{F}_{ij}^{pore}$	The forces of the jth fluid bubble applied on the ith solid particle
$\mathbf{F}^{pore}$	The vector of the solid particle forces induced from pore pressure of all the fluid bubbles
$\mathbf{F}_R$	The vector of external forces applied at all the particles
$\mathbf{H}_{global}$	The global flux pressure matrix
$\mathbf{H}_{pipe}$	The flux pressure matrix of a fluid pipe
k	The permeability of a material
k_n	The normal stiffness of a bond
k^p	The permeability of the pipe
k_s	The shear stiffness of a bond
$\mathbf{K}_{bond}$	The bond stiffness matrix under the local coordinate system
$\mathbf{K}^b$	The element stiffness matrix of each bond under the global coordinate system
$\mathbf{K}_{global}$	The global stiffness matrix
l_i	The length of the ith bond
l^p	The length of the fluid pipe
$l_{ij}^{\Gamma_0}$	The length of the straight line interface between the ith particle and jth fluid bubble
M	The number of pipes contained within V
$\mathbf{M}_{global}$	The global matrix of the fluid discharges and variation of fluid bubble pressures
n_p	The porosity
n_i^{pipe}	The ith component of unit vector directed along the pipe
n_x	The x component of the normal direction vector of the bond

n_y	The y component of the normal direction vector of the bond
$\mathbf{n}^\Gamma$	The outer normal vector of the fluid–solid interface
$\mathbf{n}_{ij}^{\Gamma_0}$	The outer normal of the straight line interface between the ith particle and jth fluid bubble
N_i^e	The element shape function associated with particle i
$N_{i,x}$	The diffusive derivative of the shape function N_i in x direction
$N_{i,y}$	The diffusive derivative of the shape function N_i in y direction
p	The pore water pressure
p_i	The fluid pressure of the ith bubble
Δp	The pressure difference across the pipe
$\mathbf{P}$	The vector of pore pressure of the fluid bubbles
$\dot{\mathbf{P}}$	The vector of variation of fluid bubble pressures
q_i	The fluid flux of the ith bubble
q_i^{macro}	The macroscopic fluid flux
q_{ji}^{move}	The fluid discharge of the jth fluid bubble caused from the movement of the ith particle
q^p	The fluid discharge caused by the variation of pressure
q_i^{pipe}	The fluid flux through the pipe in the ith direction
$\langle q_i \rangle$	The average fluid flux in the ith direction of a given volume V
Q^{pipe}	The discharge in the pipe
$\mathbf{Q}$	The vector of bubble fluid flux
$\mathbf{Q}^{\text{move}}$	The vector of the fluid discharge induced from the particle movements
$\mathbf{Q}^{\text{pressure}}$	The vector of the fluid discharges induced from variation of fluid bubble pressures
$\mathbf{Q}_R$	The vector of external discharges of the fluid bubbles
r	The distance between a point and the reference point
r_{max}	The maximum distance between the reference point and the particles (nodes)
$\mathbf{s}$	The strain vector composed of the three strain components of a spring bond
t_D	The dimensionless time
Δt	The time step
$\mathbf{T}$	The transform matrix
u_i	The displacement in x direction of particle i
$\hat{u}^n$	The normal deformation of a bond
$\hat{u}^s$	The shear deformation of a bond
$\mathbf{u}$	The displacement vector of the particles
$\hat{\mathbf{u}}$	The vector of local deformation of a spring bond
v_i	The displacement in y direction of particle i
x_i	The x coordinate of the ith particle (node)
$\mathbf{x}_{m1}$	The middle point of the spring bond i–k

$\mathbf{x}_{m2}$	The middle point of the spring bond i–l
y_i	The y coordinate of the ith particle (node)
$\dot{\mathbf{u}}_i$	The velocity vector of the ith particle
$\mathbf{U}$	The vector of particle displacements of all the particles
$\dot{\mathbf{U}}$	The vector of particle velocities of all the particles
V	The volume of the model

Greek Symbols

α	The growth factor of time step ($\alpha \geq 1.0$)
α^{2D}	A coefficient determined by the geometry data of the lattice model
δ	The effective contact area ratio between solid particle and fluid bubble
δ_t^*	The limit value the bond's stretching
η	A variable defined as $\eta = \left(\frac{A^p k^p}{\mu}\right)^{-1}$
μ	The dynamic viscosity of the fluid
v	The Poisson's ratio
$\Delta\sigma$	The applied surcharge

Miscellaneous Symbols

Δ	The unit length in the third dimension
Γ_{ij}	The interface between the ith solid particle and jth fluid bubble
$d\Gamma$	The differential contact area between fluid bubble and solid particle
$d\Gamma^*$	The differential effective contact area between fluid bubble and the solid particle
Π^b	The strain energy of the bond

1 Introduction

The origin of lattice models can be traced back to the work of Hrennikoff (1941). He demonstrated that a regular triangular lattice of bars (a truss) was capable of solving problems of continuum elasticity with Poisson's ratio fixed at 1/3. However, the method had little success due to the limited power of computers at that time. After the introduction of the finite-element method (FEM) (Clough 1960), which has become the mainstream numerical method in the engineering sciences, lattice-based models were totally abandoned since the FEM could achieve an almost exact solution using a finite number of elements. However, in recent years, there has been renewed interest in lattice/discrete numerical modeling techniques (e.g., Darve and Nicot 2005; Hahn et al. 2010), as they are well suited for modeling of cracking and failure. In the past few decades, a family of lattice models have been developed, for example, the rigid body–spring network model developed by Kawai (1978), the simple deformable polygonal

discrete-element model (DEM) (Mustoe 1992), the Born spring model (Parisi and Caldarelli 2000), the confinement-shear lattice model of Cusatis et al. (2003), the bonded-particle model (Potyondy and Cundall 2004), the explicit quasistatic lattice model (Kozicki and Tejchman 2008), the hybrid lattice particle modeling approach (Wang et al. 2009), and the distinct lattice spring model (DLSM) (Zhao 2010; Zhao et al. 2011a, b). These models have the following characteristics in common: (1) materials are discretized into particles that are connected through spring-type forces, (2) the mechanical response is derived from the microscopic or mesoscopic interactions between particles, (3) material failure/cracking at the continuous level is captured naturally from the spring failure at the discrete level, and (4) complex constitutive relationships and contact mechanisms are readily implemented. A literature review on the development of lattice models can be found in Ostoja-Starzewski (2002) and Zhao (2010).

Many important geomechanics problems involve coupled processes, e.g., hydromechanical, thermomechanical, and chemomechanical processes; For instance, hydrofracturing is an important geological process induced by high pore fluid pressures with the development of fractures controlling the permeability of geomaterials. Lattice models have several advantages for such problems, since the models can take into account the inherently discontinuous and heterogeneous nature of the geomaterial and the particle contact physics is directly resolved and is robust (Boutt et al. 2011). A few lattice-based models have been developed to solve coupled fluid flow and deformation problems. One notable approach is to model the solid using the DEM and, in the meantime, explicitly model the fluid flow using either the finite-difference method (FDM), the finite-element method (FEM), the finite-volume method (FVM), or the lattice Boltzmann (LB) method. The original work in this area was done by Tsuji et al. (1993), where the continuity and Navier–Stokes equations were solved using the FDM in Eulerian Cartesian coordinates and the driving forces from fluid flow were applied to the particles as body forces. As the coupling between the fluid flow and the particle was achieved by applying body forces, the approach could not directly model the fluid pressures in the pores. The micromechanical lattice Boltzmann (LB) and DEM (LBDEM) approach developed by Cook et al. (2004) explicitly takes into account the interaction between particles and fluid flow. A similar contribution has also been made by Feng et al. (2007), where incompressible fluid flows and large eddy simulation (LES)-based turbulence models were considered. These models were capable of accounting for the pore-scale physics without assumptions on the continuum-scale relationship between the permeability and porosity. They were used to model small-scale fluid–particle interaction simulations, e.g., particle transport

in fluid flow (Feng et al. 2007) and sand production (Boutt et al. 2011). However, as the Navier–Stokes (NS) equations are solved explicitly, the computational cost for these models is usually very high. Moreover, as the permeability of the model is determined by the geometrical structure of the computational model, a calibration process is needed to obtain the desired macroscopic permeability for a specific geomaterial. These problems can be overcome in another approach, which uses Darcy's law to model the continuum fluid flow. One representative work is that of Sakaguchi and Muhlhaus (2000), who used a continuum model (the FVM) for analysis of the pore fluid and the lattice beam model for the solid. Similar work was done by Flekkoy and Malthe-Sorenssen (2002) to simulate hydrofracturing; here a discrete spring network was used to represent the porous medium and a continuum model was used to describe the fluid flow. Since the fluid flow was modeled using a continuum approach, these models cannot be regarded as totally lattice based. Recently, a fully coupled lattice model was developed by Jain and Juanes (2009), in which the fluid flow was represented by a discrete network of pore throats. However, the coupling between fluid flow and the solid was treated as the radius variation of solid grains, which is not physically correct or realistic for geomaterials. In addition, since the model was based on an explicit solution, a very small time step had to be adopted. Another deficiency was that when the compressibility of the fluid was taken as low or made incompressible the model became unstable. These shortcomings also apply to a greater or lesser degree in other existing coupled lattice spring models.

In this work, a new lattice model is developed for coupled fluid flow and deformation problems in geomechanics. It is based on the newly developed DLSM which overcomes some of the shortcomings of the existing lattice models, namely the Poisson's ratio limitation and parameter calibration problem (Zhao 2010; Zhao et al. 2011a, b). After the introduction of DLSM (Zhao et al. 2011a), further developments are conducted, e.g., adaptation for cluster parallelization (Zhao et al. 2011b), graphics processing unit (GPU) parallelization (Zhao and Khalili 2012), coupling with numerical manifold method (NMM) (Zhao et al. 2012), and implementation of high-order DLSM (Zhao and Zhao 2012). Note that cluster parallelization and GPU parallelization are two distinct approaches in high-performance computing, and the coupled DLSM in (Zhao et al. 2012) is a continuum–discontinuum numerical method to couple NMM and DLSM. The current work is totally different from the previous ones. It is the first time that the DLSM has been developed for coupled fluid flow and deformation problems. The model adopts springs to represent the solid and fluid bubbles, connected by fluid pipelines for the fluid. The interaction between fluid and

solid is derived using boundary integration of the true fluid pressure applied on the fluid–solid interface rather than using Biot's formulation (Biot 1941). Based on the principle of DLSM, a set of discrete model-based equations are developed to interpret Biot's formulation. Based on the relationships derived between the permeability and discrete model parameters, the new lattice-based fluid flow and mechanical coupled model inherits the advantages of the DLSM on free calibration. To verify the application of the model, several numerical examples with analytical solutions are analyzed. The discrete properties and advantages of the model for solving fluid flow and deformation coupled problems in geomechanics are also discussed.

2 The Model

2.1 Solid Component

In DLSM (Zhao 2010; Zhao et al. 2011a), the material is represented by a distribution of particles linked through bonds; it includes a normal spring and a shear spring for each pair of particles. The deformation of the springs is evaluated by using the local strain rather than the particle displacements. It has been proven that this technique makes the model rotationally invariant and allows one to overcome the restriction on the Poisson's ratio in the classical lattice spring models. For two-dimensional DLSM, the lattice network can be represented by the edges of a triangular FEM mesh, in which the material is discretized into polygon particles (Fig. 1a). The complex contacts between these polygon particles are simplified as the bond contact spring between circular particles; i.e., only a single pair of bond springs is formed between two linked particles. In DLSM, the strain has to be calculated, and for the purpose of rotationally invariance, each bond is allocated to a cluster of particles. Two kinds of bonds are adopted in this work: one for bonds forming the boundary of the domain, and the other for internal bonds, as shown in Fig. 1b and c, respectively. The global stiffness matrix is assembled by the element stiffness matrix contributed by each bond, which can be obtained from the energy-minimization principle.
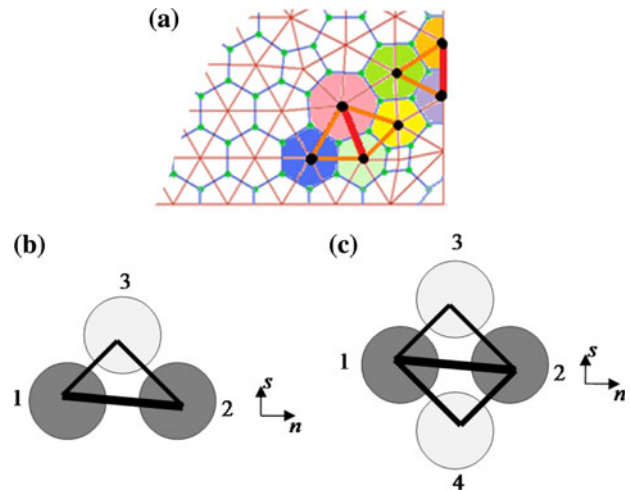
Firstly, the strain energy stored in each bond is

$$\Pi_b = \frac{1}{2} \hat{\mathbf{u}} \, \mathbf{K}_{bond} \hat{\mathbf{u}}^T, \tag{1}$$

where $\hat{\mathbf{u}} = (\hat{u}^n, \hat{u}^s)^T$ is the normal and shear deformation vector of the bond, and $\mathbf{K}_{bond}$ is the bond stiffness matrix at the local coordinate:

$$\mathbf{K}_{bond} = \begin{bmatrix} k_n & 0 \\ 0 & k_s \end{bmatrix}, \tag{2}$$

where k_n is the normal stiffness and k_s is the shear stiffness.

Fig. 1 The two types of bond in DLSM: **a** lattice model represented by FEM mesh, **b** type I: three-particle bond, and **c** type II: four-particle bond

In DLSM, the normal and shear deformation of the bond are calculated from the local strain of the bond:

$$\hat{\mathbf{u}} = \mathbf{T}\mathbf{s}, \tag{3}$$

where $\mathbf{T}$ is the transform matrix given as

$$\mathbf{T} = l \begin{bmatrix} n_x^2 & n_y^2 & 2n_x n_y \\ -n_x n_y & n_x n_y & n_x^2 - n_y^2 \end{bmatrix}. \tag{4}$$

Here, $\mathbf{s} = \begin{bmatrix} \varepsilon_{xx}, \varepsilon_{yy}, \varepsilon_{xy} \end{bmatrix}^T$ is the strain vector composed of the three strain components, l is the length of the bond, n_x is the x component of the normal direction vector of the bond, and n_y is the y component of the normal direction vector of the bond. The strain vector can be calculated according to

$$\mathbf{s} = \mathbf{B}\mathbf{u}, \tag{5}$$

where $\mathbf{B}$ is the interpolation matrix of the bond and $\mathbf{u}$ is the displacement vector of the particles involved. It should be mention that Eq. (3) is equivalent to the relative displacement between two particles. Details of proof is given in Zhao (2010) and Zhao et al. (2011a).

For the type I bond (Fig. 1b), which only belongs to one triangular element, we use the common finite-element interpolation, which gives

$$\mathbf{B} = \begin{bmatrix} N_{1,x}^e & 0 & N_{2,x}^e & 0 & N_{3,x}^e & 0 \\ 0 & N_{1,y}^e & 0 & N_{2,y}^e & 0 & N_{3,y}^e \\ \frac{1}{2}N_{1,y}^e & \frac{1}{2}N_{1,x}^e & \frac{1}{2}N_{2,y}^e & \frac{1}{2}N_{2,x}^e & \frac{1}{2}N_{3,y}^e & \frac{1}{2}N_{3,x}^e \end{bmatrix}, \tag{6}$$

$$\mathbf{u} = [u_1, v_1, u_2, v_2, u_3, v_3]^T, \tag{7}$$

where N_i^e is the element shape function associated with particle i, u_i is the displacement in x direction of particle

i, and v_i is the displacement in y direction of particle i. For the type II bond (Fig. 1c), which belongs to two triangular elements, a moving least-squares (MLS) procedure (Breitkopf et al. 2000) is adopted to calculate $\mathbf{s}$. The explicit formulas of four-noded MLS shape functions using a linear basis, which is provided in Breitkopf et al. (2000), is directly employed. In this sense, we have

$$\mathbf{B} = \begin{bmatrix} N_{1,x} & 0 & N_{2,x} & 0 & N_{3,x} & 0 & N_{4,x} & 0 \\ 0 & N_{1,y} & 0 & N_{2,y} & 0 & N_{3,y} & 0 & N_{4,y} \\ \frac{1}{2}N_{1,y} & \frac{1}{2}N_{1,x} & \frac{1}{2}N_{2,y} & \frac{1}{2}N_{2,x} & \frac{1}{2}N_{3,y} & \frac{1}{2}N_{3,x} & \frac{1}{2}N_{4,y} & \frac{1}{2}N_{4,x} \end{bmatrix}, \tag{8}$$

$$\mathbf{u} = [u_1, v_1, u_2, v_2, u_3, v_3, u_4, v_4]^{\mathrm{T}}, \tag{9}$$

where $N_{i,x}$ and $N_{i,y}$ are the diffusive derivatives given by

$$N_{i,x} = \frac{w_i}{d} \sum_{j \neq i} \sum_{k > j, k \neq i} w_j w_k (y_j - y_k) \Theta(\mathbf{x}_i, \mathbf{x}_j, \mathbf{x}_k), \tag{10}$$

$$N_{i,y} = \frac{w_i}{d} \sum_{j \neq i} \sum_{k > j, k \neq i} w_j w_k (x_k - x_j) \Theta(\mathbf{x}_i, \mathbf{x}_j, \mathbf{x}_k), \tag{11}$$

with

$$\Theta(\mathbf{x}_i, \mathbf{x}_j, \mathbf{x}_k) = -x_j y_i + x_k y_i + x_i y_j - x_k y_j - x_i y_k + x_j y_k,$$

$$d = \sum_{i=1,2} \sum_{j=i+1,3} \sum_{k=j+1,4} w_i w_j w_k (\Theta(\mathbf{x}_i, \mathbf{x}_j, \mathbf{x}_k))^2,$$

where x_i and y_i are the coordinates of the ith particle (node).

The weight function $w(r)$ used in this paper is proportional to the Gauss function and is given by

$$w(r) = e^{\left(-3\hat{r}^2\right)}, \tag{12}$$

where $\hat{r} = r/r_{\max}$ with $r = \sqrt{(x_{\mathrm{m}} - x)^2 + (y_{\mathrm{m}} - y)^2}$, $(x_{\mathrm{m}}, y_{\mathrm{m}})$ as the reference point (the center of the bond in this paper) and $r_{\max}$ as the maximum distance between the reference point and the particles (nodes).

Then, according to the energy-minimization principle and the above equations, the element stiffness matrix of each bond under global coordinate system is obtained as

$$\mathbf{K}^{\mathrm{b}} = \left[\frac{\partial^2 \Pi_b}{\partial u_i \partial u_j} \right] = (\mathbf{TB})^{\mathrm{T}} \mathrm{K}_{\mathrm{bond}} \mathbf{TB}. \tag{13}$$

Finally, the global stiffness matrix can be treated in the same manner as in the standard FEM, so that the force and displacement relationship is represented as

$$\mathbf{F} = \mathbf{K}_{\mathrm{global}} \mathbf{U}, \tag{14}$$

where $\mathbf{F}$ is the vector of particle forces, $\mathbf{K}_{\mathrm{global}}$ is the global stiffness matrix, and $\mathbf{U}$ is the vector of particle displacements.

2.2 Fluid Flow Component

The fluid flow is represented by a discrete network made up from fluid bubbles and pipes (Fig. 2). Firstly, a triangular mesh is formed for the particle model, and one fluid bubble is assigned to each triangle (Fig. 2a); a micropipe is then formed between two adjacent fluid bubbles (Fig. 2b). The fluid flow variables are defined for each bubble as the fluid pressure p and fluid flux q. For each pipe, the fluid flux and pressure constitutive relationship can be obtained from Darcy's law as

$$\begin{pmatrix} q_i \\ q_j \end{pmatrix} = \mathbf{H}_{\mathrm{pipe}} \begin{pmatrix} p_i \\ p_j \end{pmatrix}, \tag{15}$$

where q_i and p_i are the fluid flux and pressure of the ith bubble, $\mathbf{H}_{\mathrm{pipe}}$ is the flux pressure matrix given by

$$H_{\mathrm{pipe}} = -\frac{k^{\mathrm{p}} A^{\mathrm{p}}}{\mu l^{\mathrm{p}}} \begin{bmatrix} 1 & -1 \\ -1 & 1 \end{bmatrix}, \tag{16}$$

where k^{p} is the permeability of the pipe, A^{p} is the cross-sectional area of the pipe, μ is the dynamic viscosity of the fluid, and l^{p} is the length of the pipe. A global flux pressure matrix can then be assembled in a similar way to the global stiffness matrix (Eq. 14) so that the flux pressure relationship can be given as

$$\mathbf{Q} = \mathbf{H}_{\mathrm{global}} \mathbf{P}, \tag{17}$$

where $\mathbf{Q}$ is the vector of bubble fluid flux, $\mathbf{H}_{\mathrm{global}}$ is the global flux pressure matrix, and $\mathbf{P}$ is the vector of bubble pressure.

2.3 The Coupling

The coupled model is made up of basic units, i.e., bubble particle clumps (Fig. 3a). For porous media, the interface between solid particle and fluid bubble is an irregular geometry. Therefore, for a given interface (Fig. 3a), the

Fig. 2 The fluid flow and deformation coupled lattice model: **a** particle model with fluid flow bubbles, and **b** the micropipe to link two fluid bubbles
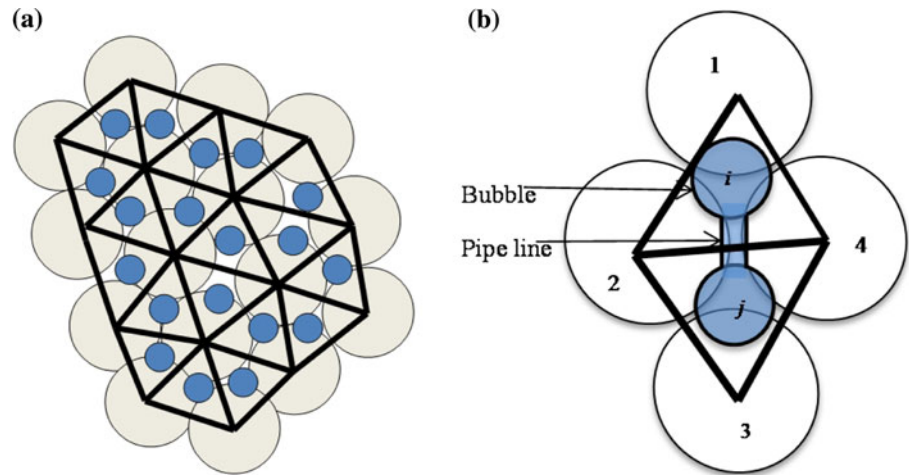
effective contact area between the fluid bubble and the solid particles may be represented as

$$d\Gamma^* = \delta d\Gamma = \frac{A_0 - A_c}{A_0} d\Gamma, \tag{18}$$

where δ is the effective contact ratio, A_0 is the total area of the interface between the fluid bubble and the solid particles, and A_c is the area of the contact between solid particles (Fig. 3a). Taking the elastic modulus of the solid particles as E_g, the elastic modulus of the porous media E_s can then be estimated as

$$E_s = E_g \frac{A_c}{A_0} \Rightarrow \frac{A_c}{A_0} = \frac{E_s}{E_g}. \tag{19}$$

The parameter δ is given as

$$\delta \approx \left(1 - \frac{E_s}{E_g}\right) = \left(1 - \frac{C_g}{C_s}\right), \tag{20}$$

where C_g and C_s are the compressibility of the solid grain and the skeleton, respectively. It can be found that δ shares the same form as Biot's coefficient.

The interaction of the fluid bubble on the solid particle is shown in Fig. 3b. Given one small segment of the

Fig. 3 Coupling between fluid flow and solid: **a** fluid bubble and particle clump, **b** pore pressure applied on solid particle, and **c** fluid flux induced by particle movement
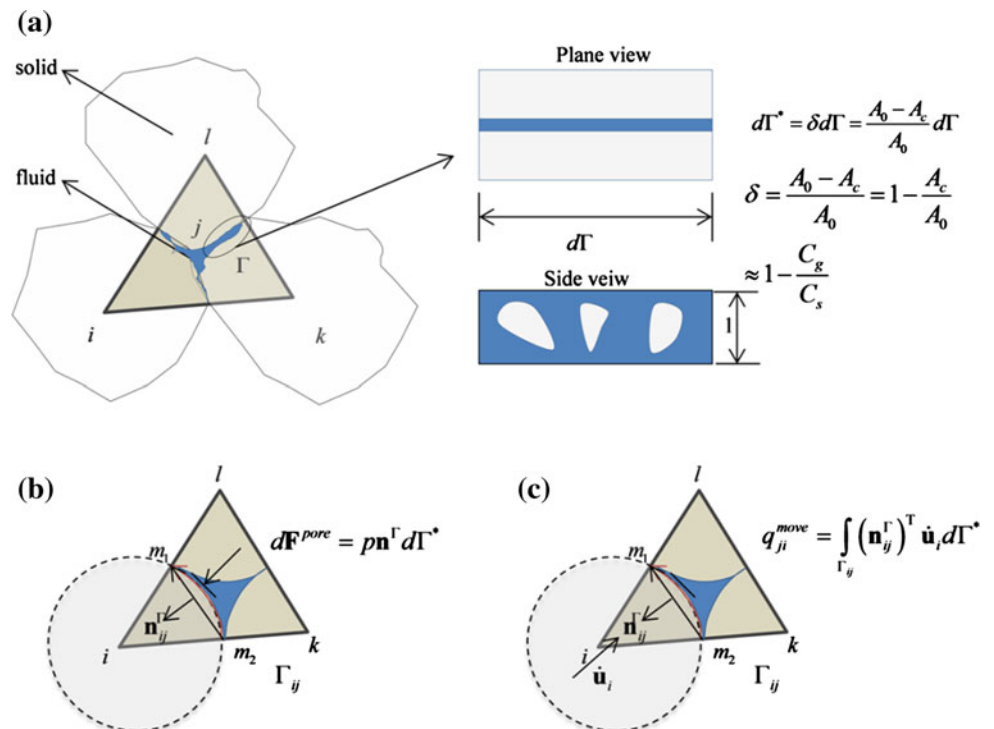
boundary of particle and fluid, the fluid pressure-induced particle force is

$$d\mathbf{F}^{\text{pore}} = p\mathbf{n}^{\Gamma}d\Gamma^*, \tag{21}$$

where p is the fluid pressure and $\mathbf{n}^{\Gamma}$ is the outer normal vector of the boundary point. Then, the forces of the jth fluid bubble applied on the ith solid particle can be given as

$$\mathbf{F}_{ij}^{\text{pore}} = \int_{\Gamma_{ij}} p_j\mathbf{n}_{ij}^{\Gamma}d\Gamma^* = \delta \int_{\Gamma_{ij}} p_j\mathbf{n}_{ij}^{\Gamma}d\Gamma. \tag{22}$$

Invoking the boundary integration property, Eq. (22) is independent of the integration path; therefore, the straight line path connected by the middle points of the spring bonds is adopted (Fig. 3b). The middle points can be obtained as

$$\mathbf{x}_{\text{m1}} = \frac{(\mathbf{x}_i + \mathbf{x}_k)}{2}, \quad \mathbf{x}_{\text{m2}} = \frac{(\mathbf{x}_i + \mathbf{x}_l)}{2}. \tag{23}$$

Its length is

$$l_{ij}^{\Gamma_0} = \|\mathbf{x}_{\text{m1}} - \mathbf{x}_{\text{m2}}\|. \tag{24}$$

The outer normal of the straight line is

$$\mathbf{n}_{ij}^{\Gamma_0} = \begin{pmatrix} 0 & -1 \\ 1 & 0 \end{pmatrix} \frac{\mathbf{x}_{\text{m1}} - \mathbf{x}_{\text{m2}}}{l_{ij}^{\Gamma_0}}. \tag{25}$$

Then, the particle forces induced by the fluid bubble can be written as

$$\mathbf{F}_{ij}^{\text{pore}} = \delta p_j\mathbf{n}_{ij}^{\Gamma_0}l_{ij}^{\Gamma_0} = \left(\delta l_{ij}^{\Gamma_0}\mathbf{n}_{ij}^{\Gamma_0}\right)p_j = \mathbf{C}_{ij}p_j. \tag{26}$$

Now, we can give the global pore pressure and particle force relationship as

$$\mathbf{F}^{\text{pore}} = \mathbf{C}_{\text{global}}\mathbf{P}, \tag{27}$$

where $\mathbf{F}^{\text{pore}}$ is the vector of the solid particle forces induced from pore pressure of all the fluid bubbles $\mathbf{P}$.

Now, considering the dependency of fluid flow on deformation, the relationship between particle displacement and fluid flux will be derived. The fluid flux of the fluid bubble induced from the solid particle movement is shown in Fig. 3c. The fluid discharge of the jth fluid bubble caused from the movement of the ith particle can be calculated as

$$q_{ji}^{\text{move}} = \int_{\Gamma_{ij}} \left(\mathbf{n}_{ij}^{\Gamma}\right)^{\text{T}}\dot{\mathbf{u}}_i d\Gamma^* = \delta \int_{\Gamma_{ij}} \left(\mathbf{n}_{ij}^{\Gamma}\right)^{\text{T}}\dot{\mathbf{u}}_i d\Gamma, \tag{28}$$

where $\dot{\mathbf{u}}_i$ is the velocity vector of the ith particle.

Again, based on the property of boundary integration, this can be given as

$$q_{ji}^{\text{move}} = \delta l_{ij}^{\Gamma_0}\left(\mathbf{n}_{ij}^{\Gamma_0}\right)^{\text{T}}\dot{\mathbf{u}}_i^* = \left(\delta l_{ij}^{\Gamma_0}\left(\mathbf{n}_{ij}^{\Gamma_0}\right)^{\text{T}}\right)\dot{\mathbf{u}}_i = \mathbf{C}_{ij}^{\text{T}}\dot{\mathbf{u}}_i, \tag{29}$$

and the global relationship becomes

$$\mathbf{Q}^{\text{move}} = \mathbf{C}_{\text{global}}^{\text{T}}\dot{\mathbf{U}} \tag{30}$$

where $\mathbf{Q}^{\text{move}}$ is the vector of the fluid discharge induced from particle movements, and $\dot{\mathbf{U}}$ is the vector of particle velocities.

The variation of pressure will also cause fluid discharge for the bubble, and this can be given according to the compressibility relationship of the fluid,

$$q^p = \int_{\Omega} c_{\text{f}}\dot{p}d\Omega = n_{\text{p}}A^{\text{ele}}c_{\text{f}}\dot{p}, \tag{31}$$

where c_{f} is the compressibility of the fluid, n_{p} is the porosity, and A^{ele} is area of the triangle which contains the fluid bubble.

Equation (31) can be rewritten into the global relationship as

$$\mathbf{Q}^{\text{pressure}} = \mathbf{M}_{\text{global}}\dot{\mathbf{P}}, \tag{32}$$

where $\mathbf{Q}^{\text{pressure}}$ is the vector of the fluid discharges induced from variation of fluid bubble pressures, $\mathbf{M}_{\text{global}}$ is the global matrix of the fluid discharge and variation of fluid bubble pressures, and $\dot{\mathbf{P}}$ is the vector of variation of fluid bubble pressures.

Applying the equilibrium condition for the solid and mass balance conditions of fluid flow, we obtain the following global equations:

$$\mathbf{K}_{\text{global}}\mathbf{U} + \mathbf{C}_{\text{global}}\mathbf{P} = \mathbf{F}_R, \tag{33}$$

$$\mathbf{C}_{\text{global}}^{\text{T}}\dot{\mathbf{U}} - \mathbf{H}_{\text{global}}\mathbf{P} - \mathbf{M}_{\text{global}}\dot{\mathbf{P}} = \mathbf{Q}_R, \tag{34}$$

where $\mathbf{F}_R$ is the vector of external forces applied at the particles, and $\mathbf{Q}_R$ is the vector of external discharges of the fluid bubbles.

These equations share the same form as Biot's governing differential equations (Biot 1941) and can be viewed as a discrete interpretation of Biot's equations. Based on the
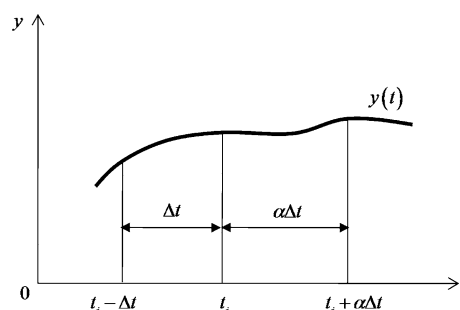

Fig. 4 The three-point method for temporal discretization

discrete framework model, we have derived the coupled fluid flow and deformation constitutive equations.

2.4 Temporal Discretization

The three-point discretization scheme developed by Khoshghalb et al. (2010) is adopted for the time integration of Eqs. (33) and (34). The discretization scheme is reported to have second-order accuracy and avoids spurious ripple effects. As shown in Fig. 4, the time derivative of an arbitrary function $y(t)$ can be written as

$$\dot{y}(t + \alpha\Delta t) = \frac{Ay(t + \alpha\Delta t) - By(t) + Cy(t - \Delta t)}{\Delta t}, \quad (35)$$

$$A = \frac{2\alpha + 1}{\alpha(\alpha + 1)}, \quad B = \frac{\alpha + 1}{\alpha}, \quad C = \frac{1}{B}, \quad (36)$$

where α is the growth factor of time step ($\alpha \geq 1.0$).

Applying Eq. (35) to Eqs. (33) and (34) gives

$$\mathbf{K}_{\text{global}}\mathbf{U}^{t+\alpha\Delta t} + \mathbf{C}_{\text{global}}\mathbf{P}^{t+\alpha\Delta t} = \mathbf{F}_R^{t+\alpha\Delta t}, \quad (37)$$

$$\mathbf{C}_{\text{global}}^T\left(\frac{A\mathbf{U}^{t-\Delta t} - B\mathbf{U}^t + C\mathbf{U}^{t+\Delta t}}{\Delta t}\right)$$
$$- \mathbf{H}_{\text{global}}\mathbf{P} - \mathbf{M}_{\text{global}}\left(\frac{A\mathbf{P}^{t-\Delta t} - B\mathbf{P}^t + C\mathbf{P}^{t+\Delta t}}{\Delta t}\right)$$
$$= \mathbf{Q}_R^{t+\alpha\Delta t}. \quad (38)$$

Then, the overall matrix equation of the system is expressed as

$$\begin{bmatrix} \mathbf{K}_{\text{global}} & \mathbf{C}_{\text{global}} \\ \mathbf{C}_{\text{global}}^T & -\left(\frac{\Delta t}{A}\mathbf{H}_{\text{global}} + \mathbf{M}_{\text{global}}\right) \end{bmatrix}\begin{bmatrix} \mathbf{U}^{t+\alpha\Delta t} \\ \mathbf{P}^{t+\alpha\Delta t} \end{bmatrix} = \begin{bmatrix} \mathbf{F}_R^{t+\alpha\Delta t} \\ \frac{1}{A}\left(\Delta t\mathbf{Q}_R^{t+\alpha\Delta t} + B\mathbf{C}_{\text{global}}^T\mathbf{U}^t - C\mathbf{C}_{\text{global}}^T\mathbf{U}^{t-\Delta t} - B\mathbf{M}_{\text{global}}\mathbf{P}^t + C\mathbf{M}_{\text{global}}\mathbf{P}^{t-\Delta t}\right) \end{bmatrix}. \quad (39)$$

For the first time step, let $\mathbf{U}^0 = 0$, $\mathbf{P}^0 = 0$, and $A = 1$, $B = 1$, $C = 0$, which is the two-point backward time integration scheme, so that Eq. (39) can be solved. Subsequently, the system equation will be solved based on the results of the two previous time steps.

2.5 Relationship Between Micro and Macro Parameters

The relationship between the spring parameters k_n, k_s and the elastic constants, i.e., the Young's modulus E and the Poisson's ratio v, is given as follows (Zhao 2010; Zhao et al. 2011a) for plane-stress problems:

$$k_n = \frac{2E}{\alpha^{2D}(1-v)},$$
$$k_s = \frac{2(1-3v)E}{\alpha^{2D}(1-v^2)}, \quad (40)$$

and as

$$k_n = \frac{2E}{\alpha^{2D}(1+v)(1-2v)},$$
$$k_s = \frac{2(1-4v)E}{\alpha^{2D}(1+v)(1-2v)} \quad (41)$$

for plane-strain problems. Given the geometry data of the lattice spring model, α^{2D} can be estimated through

$$\alpha^{2D} = \frac{\sum l_i^2}{\bar{A}\Delta}, \quad (42)$$

where l_i is the original length of the ith bond, $\bar{A}$ is the area of the model, and Δ is the unit length in the third dimension. Equations (40) and (41) are then used to estimate the two spring stiffnesses of the DLSM for numerical simulation of elastic problems.

A similar relationship between the parameter of the fluid pipe and macroscopic permeability can be derived. Firstly, the macro Darcy's law is written as

$$q_i^{\text{macro}} = -\frac{k_{ij}}{\mu}\frac{\partial p}{\partial x_j}, \quad (43)$$

where k_{ij} is the macroscopic permeability and μ is the dynamic viscosity of the fluid.

Darcy's law for the fluid pipe can be written as

$$q^{\text{pipe}} = \frac{-k^p A^p}{\mu}\frac{(p_j - p_i)}{l^p} = -\frac{(p_j - p_i)}{\eta l^p}, \quad \eta = \left(\frac{A^p k^p}{\mu}\right)^{-1}, \quad (44)$$

where q^{pipe} is the fluid flux through the pipe, k^p is the permeability of the pipe, A^p is the cross-sectional area of the pipe, and l^p is the length of the pipe.

The average fluid flux in a volume V is defined as (Fig. 5):

$$\langle q_i \rangle = \frac{1}{V}\int_V q_i^{\text{pipe}}\mathrm{d}V, \quad (45)$$

where q_i^{pipe} is the fluid flux of the ith direction through the pipe. By restricting the flow of fluid to the fluid pipes, the integral can be replaced by a summation over all M pipes contained within V:

$$\langle q_i \rangle = \frac{1}{V} \sum_{p=1}^{M} q_i^{\text{pipe}} V^{\text{p}} = \frac{1}{V} \sum_{p=1}^{M} q_i^{\text{pipe}} A^{\text{p}} l^{\text{p}}. \tag{46}$$

The flow flux in a pipe is given by

$$q_i^{\text{pipe}} = \frac{Q^{\text{pipe}} n_i^{\text{pipe}}}{A^{\text{p}}}, \tag{47}$$

where Q^{pipe} is the discharge in the pipe and n_i^{pipe} is the ith component of unit vector directed along the pipe. After substitution of Eq. (44), the flow flux becomes

$$q_i^{\text{pipe}} = -\frac{\Delta p \, n_i^{\text{pipe}}}{\eta \, l^{\text{p}} A^{\text{p}}}, \tag{48}$$

where Δp is the pressure difference across the pipe. If the mean pressure gradient in the material, $\frac{\partial p}{\partial x_j}$, is assumed to apply at the fluid pipe level, within each pipe, then

$$\Delta p = l^{\text{p}} \sum_{j=1}^{3} n_j^{\text{pipe}} \frac{\partial p}{\partial x_j}. \tag{49}$$

Then, the average fluid flux measured in the fluid pipe represented domain is given as

$$\langle q_i \rangle = -\left[\frac{1}{V} \sum_{p=1}^{M} \frac{l^{\text{p}} n_i^{\text{pipe}} n_j^{\text{pipe}}}{\eta} \right] \frac{\partial p}{\partial x_j}. \tag{50}$$

By comparing this expression with the macroscopic Darcy's law, we find that the fluid conductivity tensor of the microstructure model is given by

$$k_{ij} = \mu \frac{1}{V} \sum_{p=1}^{M} \frac{l^{\text{p}} n_i^{\text{pipe}} n_j^{\text{pipe}}}{\eta}. \tag{51}$$

Given a bubbles and pipes model, the values of the fluid flow conductivity tensor can be computed using Eq. (51).

In an isotropically permeable material, the permeability tensor can be expressed in terms of a single parameter, k, such that $k_{ij} = k\delta_{ij}$. For such a material, and assuming uniform η for all pipes, we have

$$\begin{aligned}
k &= \frac{1}{3}(k_{11} + k_{22} + k_{33}) \\
&= \frac{\mu}{3V\eta} \sum_{j=1}^{M} l_j^{\text{p}} \left(\left(n_{j\_1}^{\text{pipe}} \right)^2 + \left(n_{j\_2}^{\text{pipe}} \right)^2 + \left(n_{j\_3}^{\text{pipe}} \right)^2 \right) \\
&= \frac{\mu}{3V\eta} \sum_{j=1}^{M} l_j^{\text{p}},
\end{aligned} \tag{52}$$

where μ is the dynamic viscosity of the fluid, V is the volume of the model, η is defined in Eq. (44), l^{p} is the length of the pipe, and M is the number of pipes in the model.

This can be rewritten to express η in terms of k as

$$\eta = \frac{\mu}{3kV} \sum_{j=1}^{M} l_j^{\text{p}}. \tag{53}$$

For the two-dimensional case, this equation can be written as

$$\eta = \frac{\mu}{2k\bar{A}\Delta} \sum_{j=1}^{M} l_j^{\text{p}}. \tag{54}$$

The fluid flow parameter for the pipe can then be obtained directly according to Eqs. (52) and (54) once the permeability k is known. This guarantees that the coupled DLSM keeps the benefit of directly using conventional parameters for discrete modeling.

Fig. 5 Representation of macro continuum fluid flow using a micro model for (**a**) macro continuum element, and (**b**) micro pipe network

$$q_i^{macro} = -\frac{k_{ij}}{\mu} \frac{\partial p}{\partial x_j} \qquad \langle q_i \rangle = \frac{1}{V} \sum_{p=1}^{M} q_i^{pipe} V^P$$
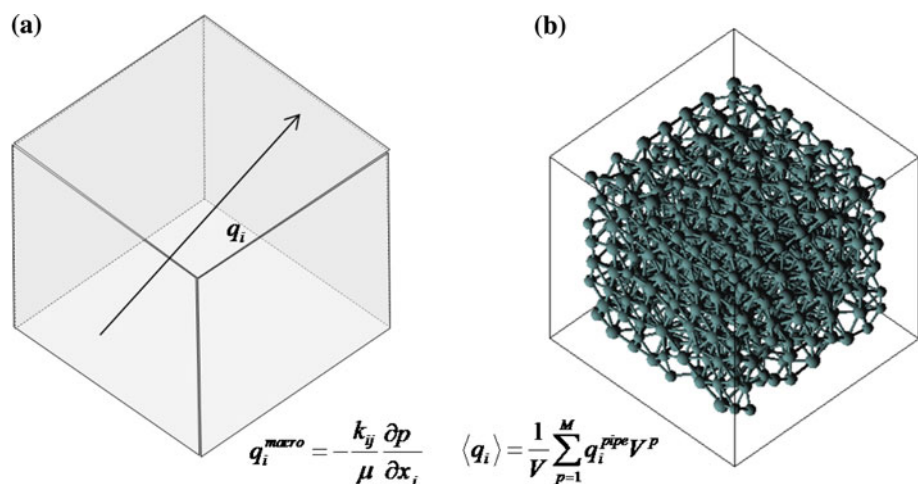
Fig. 6 One-dimensional Terzaghi's consolidation problem: **a** physical model, and **b** DLSM model
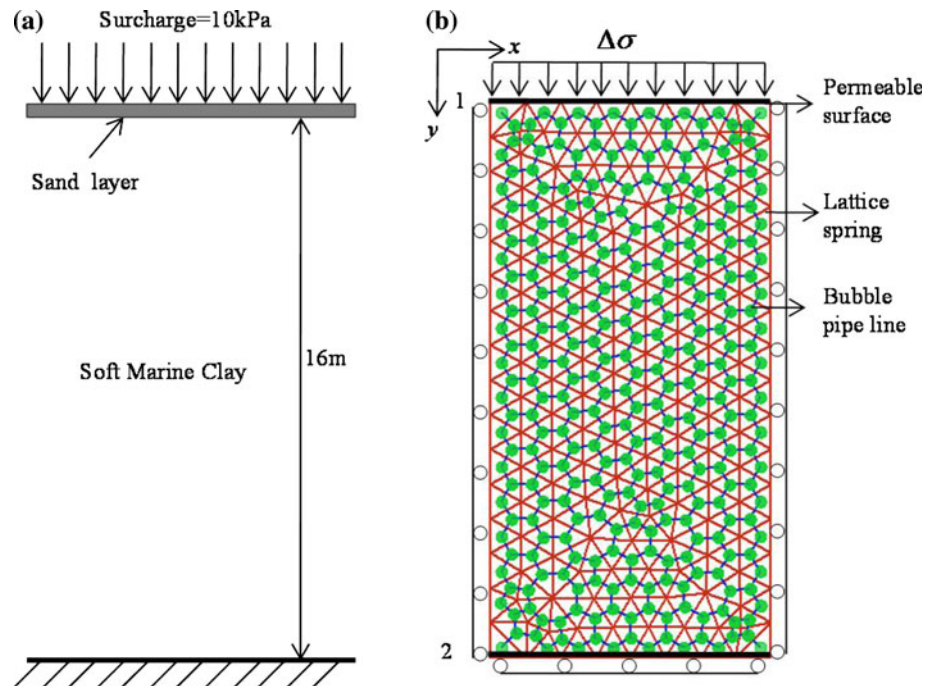
3 Verification

3.1 One-Dimensional Consolidation Problem

The problem posed and the lattice computational model used are shown in Fig. 6. A surcharge of 10 kPa is applied at the upper surface. The bottom and two side boundaries of the model are impervious and fixed for displacements in the y and x directions, respectively. The parameters of the

Fig. 7 Surface settlement and pore pressure curve of DLSM and comparison with the closed-form solution

soil are taken as $E = 40{,}000$ kPa, $v = 0.3$, $\mu = 10^4 \text{N/m}^3$, and $k = 1.728 \times 10^{-3}$ m/day. The porosity is taken as 0.5. The analytical solutions for pore water pressure and surface settlement are given by Terzaghi and Peck (1976) as

$$p = \frac{4}{\pi}\Delta\sigma \sum_{n=1}^{\infty} \frac{1}{2n-1} \sin\left(\frac{(2n-1)\pi y}{2H}\right) e^{-(2n-1)^2\frac{\pi^2}{4}T_V}, \quad (55)$$

$$s_t = m_v \Delta\sigma H \left(1 - \frac{8}{\pi^2}\sum_{n=1}^{\infty}\frac{1}{2n-1}e^{-(2n-1)^2\frac{\pi^2}{4}T_V}\right), \quad (56)$$

where the parameters are defined as

$$T_V = \frac{C_V}{H^2}t, \quad C_V = \frac{k}{\gamma_w m_v}, \quad m_v = \frac{(1+v)(2-2v)}{E(1-v)}. \quad (57)$$

The time step is taken as 0.1 days, and the growth factor α is taken as 1.1. The numerical results of the DLSM for the surface settlement and excess pore water pressure at the bottom are compared with the analytical solutions from Eqs. (55) and (56) in Fig. 7; good agreement between the numerical and analytical solutions is achieved. The lattice network model gives a larger estimation of the spring stiffness and permeability resistance of the pipelines (smaller permeability), which results in a model with slightly stiffer response and lower permeability. For this reason, in Fig. 7, the settlement is slightly underestimated and the pore pressure is slightly overestimated at a given time. It should be mentioned that, with increasing number of particles, this difference decreases dramatically. The fluid was treated as incompressible in this section ($c_f = 0.0$), which demonstrates the ability of the proposed model to capture limit compressibility conditions.

Fig. 8 A realistic DLSM model: **a** DEM model, and **b** DLSM model
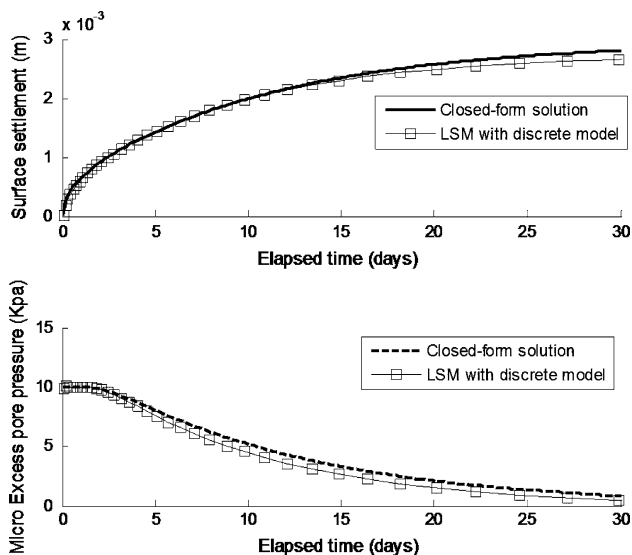
Fig. 9 Results of the realistic DLSM model for the one-dimensional consolidation problem

A realistic DLSM model is used to simulate the problem, and all material parameters are taken the same as in the previous simulation. As shown in Fig. 8, the particle model is generated using the random packing method proposed by Potyondy and Cundall (2004). The lattice model is constructed through triangulation of the particle model (Fig. 8b). The modeling results are presented in Fig. 9, deviating slightly from the analytical solution because the boundary conditions are actually applied on the particle center rather than at the boundaries of the model (Fig. 8b). This error will decrease with increasing number of particles. Figure 10 shows the variation of the force chain and displacement of the model during the consolidation process. In DLSM, porosity is an input value (0.5)

rather than an intrinsic property of the particle model. This treatment is used to avoid some limitations of the 2D particle model. There is an aforementioned issue of floating particles in two-dimensional DEM to generate high-porosity material (Hsieh et al. 2008). To overcome this problem, Hsieh et al. (2008) proposed a *porous* particle method to represent the "porous matrix." Moreover, the particle model also needs special treatment for hydraulic analysis, i.e., decreasing the particle size to fit the desired hydraulic property (Cook et al. 2004; Feng et al. 2007). In this paper, as shown in Fig. 11, it is assumed that the particle shape can be adjusted according to different porosities, and it will not influence the lattice structure and the coupling between fluid and solid due to the contour-independent property of boundary integration. It should be mentioned that, even if the macro porosity is used, the underlying calculations are still performed in a discrete manner.
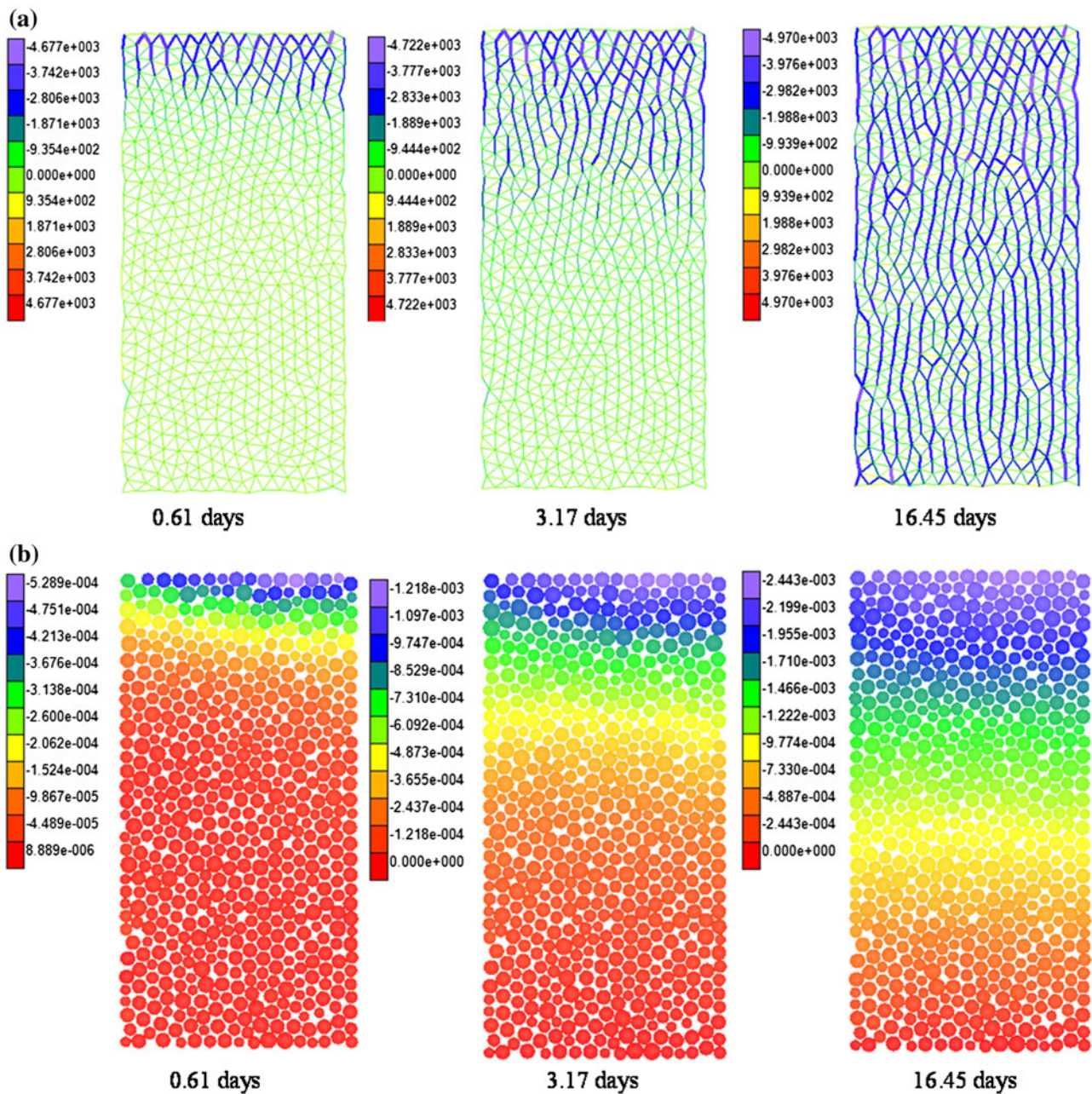
3.2 Two-Dimensional Consolidation

In this section, a two-dimensional, plane-strain consolidation problem of a clay layer subjected to a strip loading, with width of $2a$, is considered (Fig. 12). The depth of the model is taken as $9a$, and the width is assumed to be $6a$. The top surface of the model is assumed to be fully drained, while the left, right, and bottom boundaries are impervious and roller boundaries are applied to fix against their horizontal and vertical displacement. The analytical solution of this problem is given by Schiffman et al. (1969) and has been used as a verification example for FEM code (ANSYS Inc. 2010). The material parameters used will be those in ANSYS Inc. (2010) to allow direct comparison of the DLSM with both analytical and classical FEM solutions. Because of symmetry, only one-half of the medium is analyzed. The material properties used in this problem are: $E = 1,000$ Pa, $v = 0.0$, $k = 0.267 \times 10^{-4}$ m/s, $\mu = 10^4$ N/m^3, $a = 1$ m, $n_p = 0.5$, and $\Delta\sigma = 100$ Pa. The dimensionless time is defined as

$$t_D = \frac{Ek}{(1+v)\mu a^2} t. \tag{58}$$

The time step used is 227.668 s, equal to 0.0061 of the dimensionless time for this problem. The time step growth factor α is taken as 1.1. DLSM models with lattice size of 1.0, 0.5, and 0.20 m were used to model this problem. Distributions of dimensionless excess pore pressure ($p/\Delta\sigma$) against depth ratio (z/a) under the center of the strip at dimensionless time $t_D = 0.1$ are shown in Fig. 13. It was found that good correspondence between the DLSM, FEM, and analytical solutions was obtained. From this example, the ability of DLSM to model coupled fluid flow and deformation problems is further verified.

Fig. 10 Force chain and displacement at different times for the one-dimensional consolidation problem: **a** force chain, and **b** displacement in vertical direction
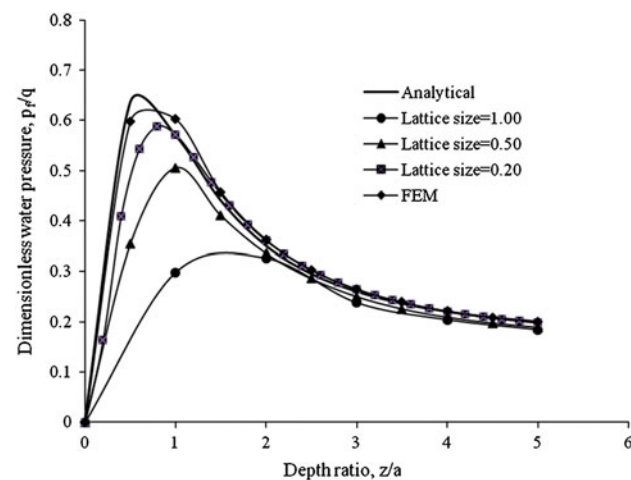
4 Discussion

4.1 Porosity

Here, DLSM models with different porosities are used to calculate the one-dimensional consolidation porous media saturated with slightly compressible water. All material parameters and boundary conditions are taken as the same as those in Sect. 3.1. The compressibility of water

is taken as $c_f = 5.1 \times 10^{-10}$ Pa^{-1}. The modeling results are shown in Fig. 14; it can be seen that the settlement of the top surface and pore pressure are only slightly influenced by the porosity. Here, the porosity $n_p = 1.0$ means a limit state where the material is made up from springs and water, e.g., a membrane tissue filled with water. The results show that the volumetric percentage of water does not have much influence on the mechanical response of a porous media. It will still behavior like a
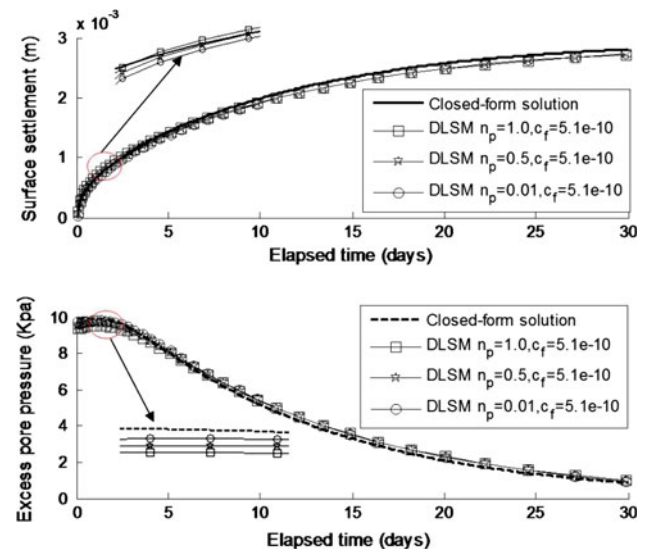
Fig. 11 Particle shapes under different porosities: **a** the intrinsic packing porosity, **b** smaller than the intrinsic value, and **c** larger than the intrinsic value
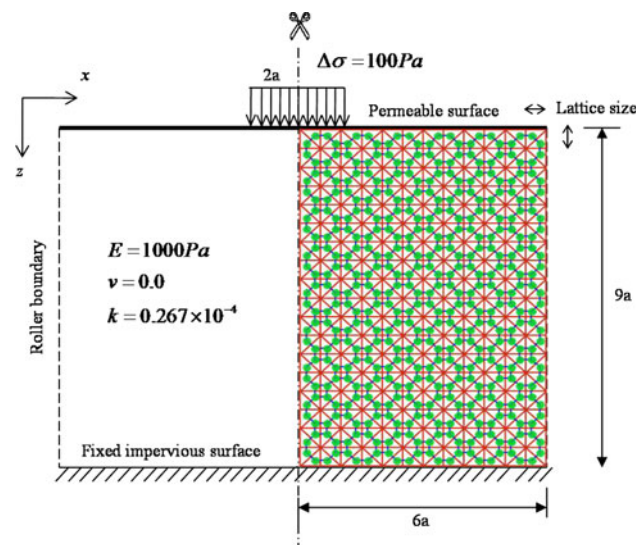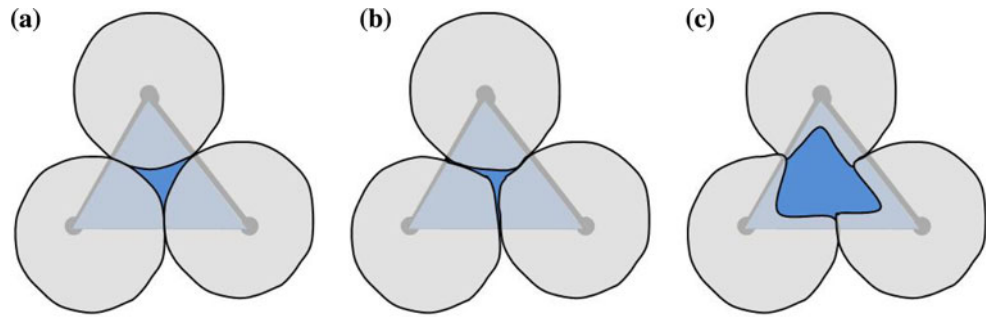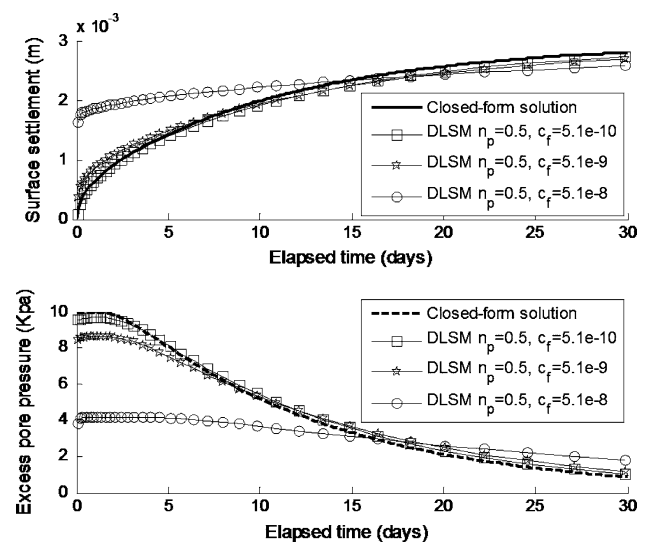

Fig. 12 Sketch of the two-dimensional consolidation problem

Fig. 14 Results of DLSM models with different porosities for the one-dimensional consolidation problem

Fig. 13 Results of DLSM models with different lattice sizes on the dimensionless excess pore pressure versus depth ratio along the center of the loaded area at $t_D = 0.1$
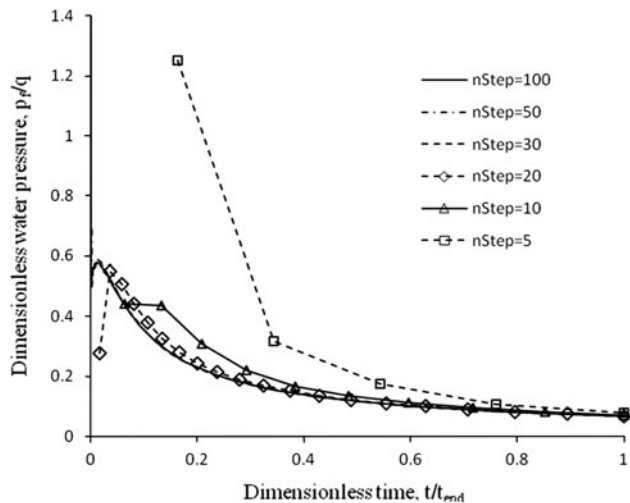

Fig. 15 Results of DLSM models with different compressibilities for the one-dimensional consolidation problem

Table 1 Calculation steps and the corresponding time step for the two-dimensional consolidation problem

Steps	100	50	30	20	10	5
Time step (s)	2.7	321.8	2,276.9	6,539.1	23,510.0	61,365.0

Fig. 16 Results of DLSM for the two-dimensional consolidation problem under different calculation steps

solid rather than a fluid even if it is fully made up from water ($n_p = 1.0$).

4.2 Fluid Compressibility

In this section, the influence of fluid compressibility is considered. DLSM models with different compressibilities ($c_f = 5.1 \times 10^{-10}$ Pa^{-1}, $c_f = 5.1 \times 10^{-9}$ Pa^{-1}, $c_f = 5.1 \times 10^{-8}$ Pa^{-1}) were calculated. The macroscopic results are presented in Fig. 15, which shows that the compressibility influences both the macroscopic pore pressure and the surface settlement. It was found that models with higher-compressibility fluid will induce larger immediate settlement followed by more gradual consolidation of the medium and lower pore pressures.

4.3 Time Step

Different time steps were used to calculate the two-dimensional consolidation problem in Sect. 3.2. The time steps used are given in Table 1, and the results are shown in Fig. 16. As can be seen, although the accuracy of the results reduces dramatically with increasing time step, they are stable in the entire range of the steps used. This advantage of time step stability is due to the implicit scheme and the three-point time integration method adopted in the model.

4.4 Fracture Simulation

A specific fracture simulation was solved to illustrate the advantages of the coupled DLSM for solving complex failure problems under coupled fluid flow and deformation conditions. The geometry and loading setup of the model are shown in Fig. 17, in which the lattice size is taken as 4 m. The applied pressure on the notch surfaces is 10 MPa. The elastic constants of the material are $E = 10^3$ MPa and $v = 0.2$, the porosity is taken as $n_p = 0.1$, and the macroscopic permeability is $k = 1.732 \times 10^{-3}$ m/day. Again, the spring parameters and pipe parameter are obtained according to Eqs. (41) and (54). The purpose of this example is to show the ease with which the model can simulate fracture processes. We only consider the tensile failure of a bond, which occurs when

$$\hat{u}_n > \delta_t^*, \tag{59}$$

where $\hat{u}_n$ is the normal deformation and δ_t^* is the limit value of the bond's stretching (0.025 m for all the simulations in this section). More sophisticated bond fracture criteria can be developed and implemented for more realistic modeling of the fracture processes. The time step is taken as 0.1 days, the growth factor α is taken as 1.1, and 20 cycles are performed in total. The most simple and direct method to deal with fracturing is to directly delete failure bonds from the calculation procedure. The results of the failure pattern under different steps are shown in Fig. 18. The bond where failure occurs is marked by double red lines around the center of the bond. It can be
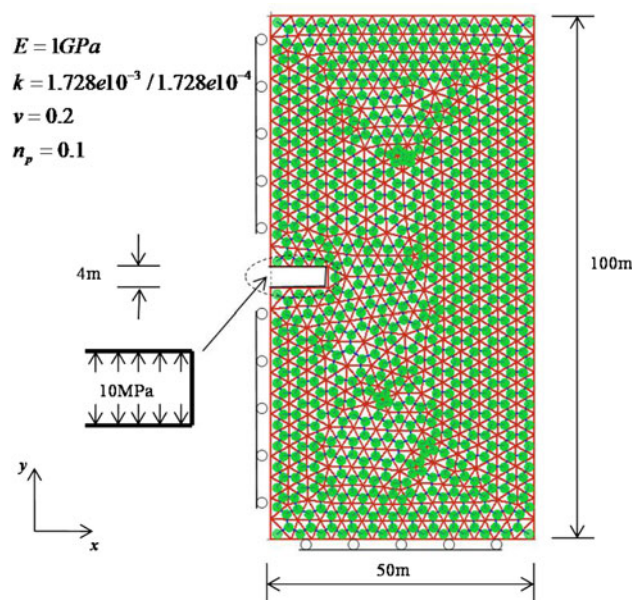
Fig. 17 Geometry and boundary conditions for fracture simulation under coupled fluid flow and deformation conditions (all boundaries are impervious)

Fig. 18 The fracture process predicted by DLSM using the bond deleting method: **a** step = 5, **b** step = 10, **c** step = 15, and **d** step = 19
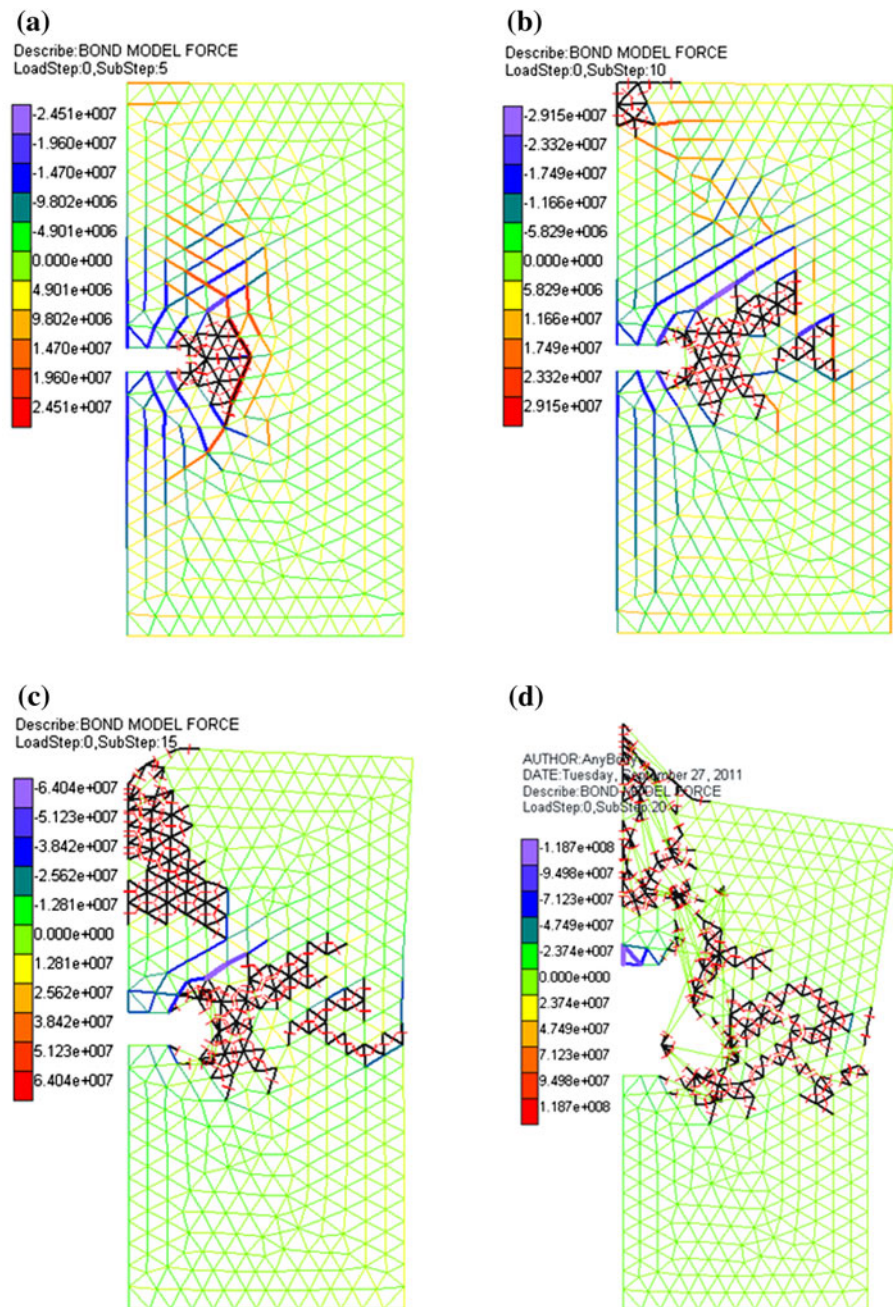
seen that the model collapses at 20 steps. In the next simulation, the contact behavior of the bond is considered. The modeling results are shown in Fig. 19. With regard to the crack patterns obtained, the simulation gives a realistic description of the fracture process and a stable result. Therefore, we can conclude that the contact between particles is essential for predicting a reasonable fracture pattern. The treatment of the contact between failure elements is also one of the advantages of the DLSM over FEM. The influence of fluid flow behavior on fracturing was also studied. Figure 20 presents the results of a lattice model with low macroscopic permeability ($k = 1.732 \times 10^{-4}$ m/day). A different fracture pattern was obtained, which means that the fluid flow property of the model influences the failure patterns. In the previous simulations, the influence of failure on the fluid flow behavior is not considered. Therefore, we set the permeability of the related failure pipes as 100 times its original value. The modeling results are shown in Fig. 21. Compared with Fig. 19, we see that a different fracture path is obtained; the change of fluid flow caused by fracturing also influences the fracturing in return. Thus, fracturing in coupled

Fig. 19 The fracture process predicted by DLSM with contact treatment of the failure bonds: **a** step = 5, **b** step = 10, **c** step = 15, and **d** step = 20
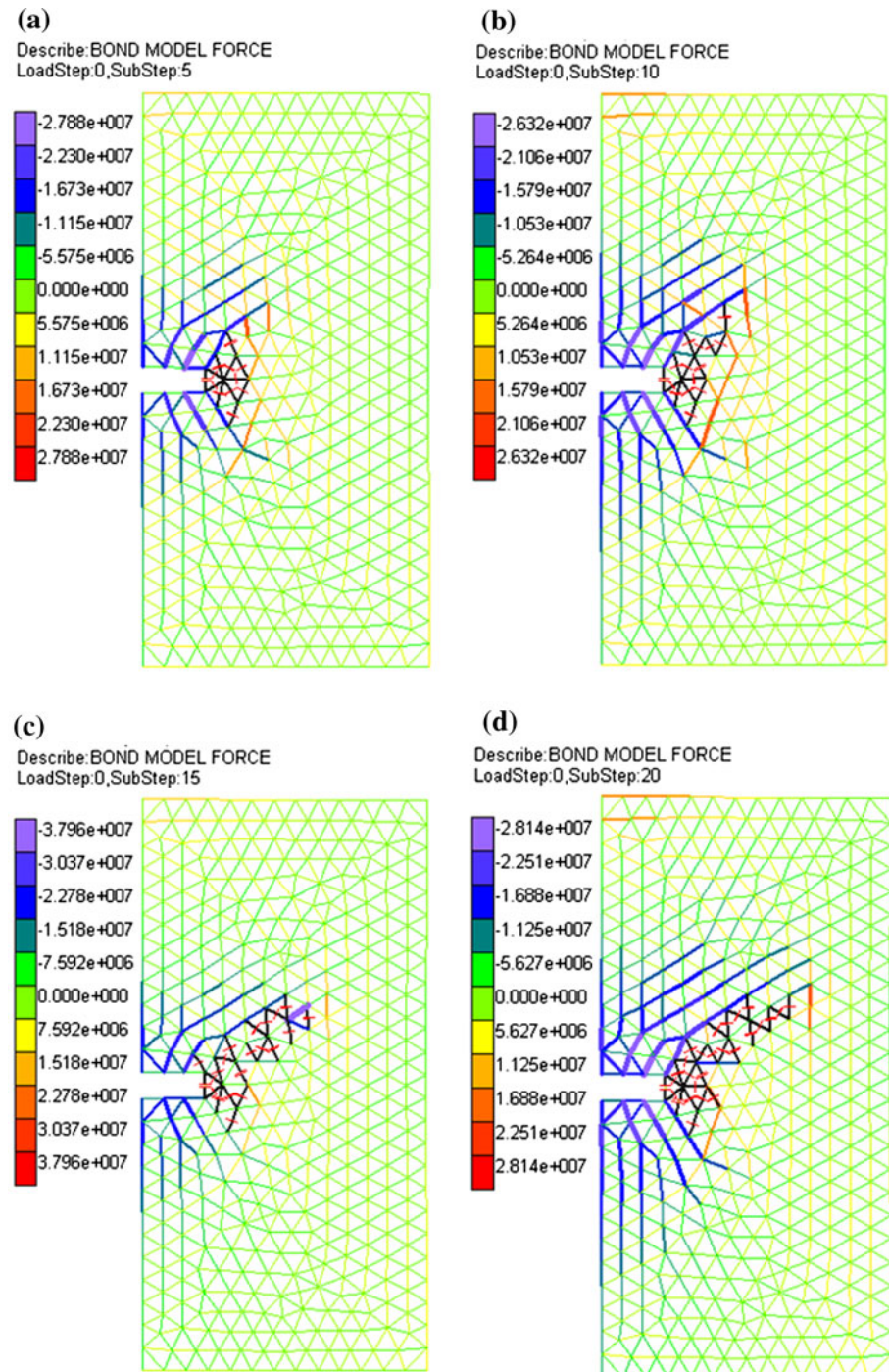
fluid flow and deformation is more complex than that in the pure mechanical condition, and a more sophisticated study on this issue is needed. Even so, from the current results we can conclude that the prediction of the failure behavior of a fluid-saturated solid requires correct modeling of the complex contact behavior, which is the major advantage of lattice models. For this reason, we believe that lattice models have great potential to model complex
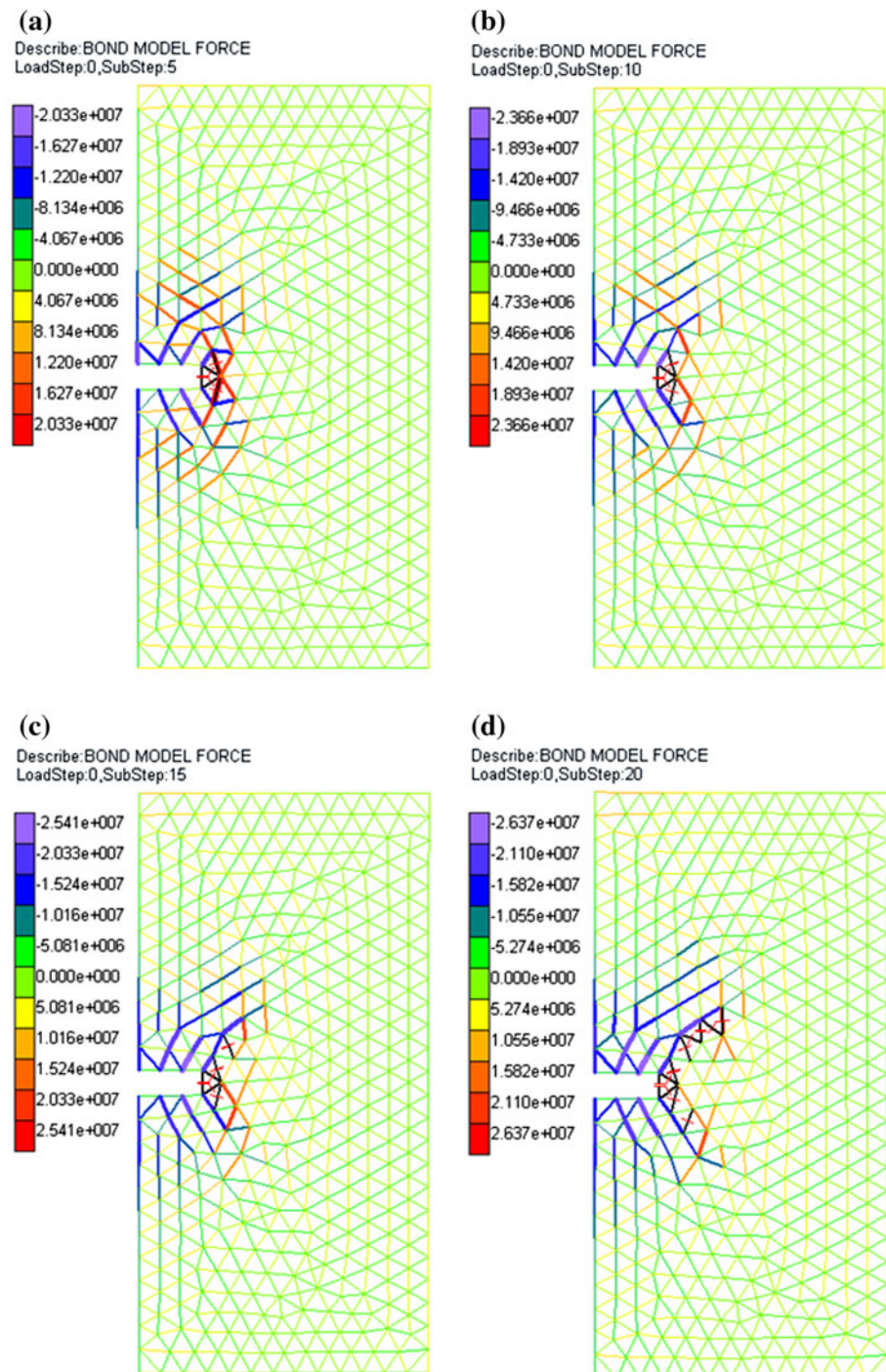
fracturing problems under coupled fluid flow and deformation conditions.

5 Conclusions

This paper presents a lattice model for coupled fluid flow and deformation problems in geomechanics. The

Fig. 20 The fracture process predicted by DLSM with low permeability: **a** step = 5, **b** step = 10, **c** step = 15, and **d** step = 20

mechanical deformation of the solid is calculated using a spring network, and the fluid flow is modeled by a fluid pipe network. Equations for the mechanical deformation, fluid flow, and coupling between them are derived. The relationship which bridges the discrete parameters and macro constants is also derived. The model is capable of capturing the fluid flow and mechanical coupled behavior of a fully saturated solid, as demonstrated numerically. It is found that there is good agreement with corresponding

analytical and FEM solutions. The influence of porosity, compressibility, lattice structure, and time step on the modeling results was studied to emphasize the advantages of the model developed in this study. It is found that incompressible fluid flow can be easily accommodated by the model and a very large time step can also be adopted. The fracture process of a notched model under pressure was also simulated by the model; results show that the proposed model is suitable and convenient to model

Fig. 21 The fracture process predicted by DLSM with treatment of the permeability of failure pipes: **a** step = 5, **b** step = 10, **c** step = 15, and **d** step = 20
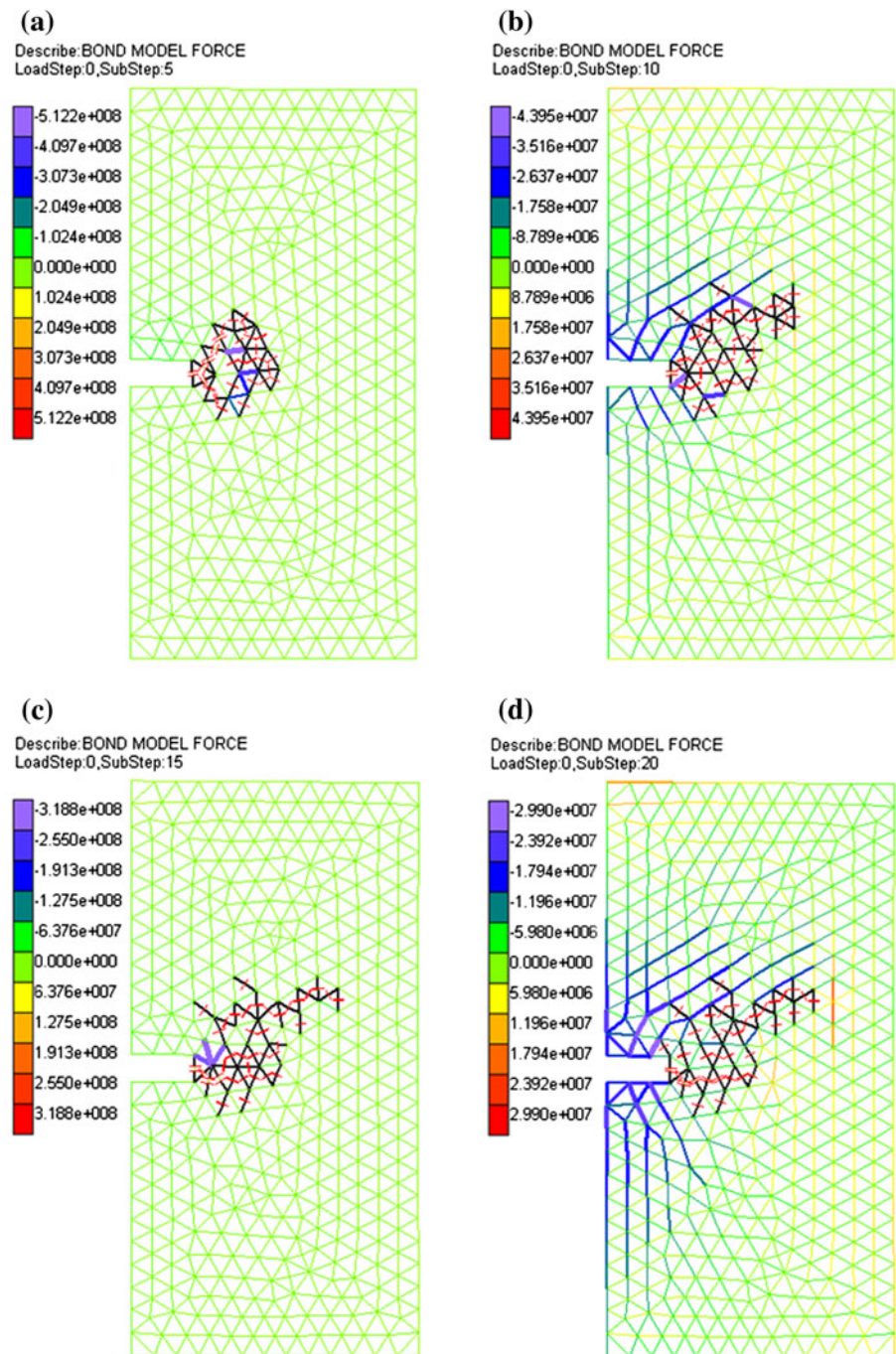
fracture under coupled fluid flow and deformation conditions.

References

ANSYS Inc (2010) VM260 two-dimensional consolidation settlement problem. ANSYS User's Manual

Biot MA (1941) General theory of three-dimensional consolidation. J Appl Phys 12:155–164

Boutt DF, Cook BK, Williams JR (2011) A coupled fluid-solid model for problems in geomechanics: application to sand production. Int J Numer Anal Meth Geomech 35:997–1018

Breitkopf P, Rassineux A, Touzot G, Villon P (2000) Explicit form and efficient computation of MLS shape functions and their derivatives. Int J Numer Meth Eng 48(3):451–466

Clough RW (1960) The finite element method in plane stress analysis. Proc Secon ASCE Conf Elec Compu, Pittsburg 345

Cook B, Nobel D, Williams J (2004) A direct simulation method for particle-fluid systems. Eng Comput 21:151–168

Cusatis G, Bažant ZP, Cedolin L (2003) Confinement-shear lattice model for concrete damage in tension and compression. I: Theory. J Eng Mech 129(12):1439–1448

Darve F, Nicot F. (2005) On incremental non-linearity in granular media: phenomenological and multi-scale views (Part I). Int J Numer Anal Meth Geomech 29:1387–1409

Feng YT, Han K, Owen DRJ (2007) Coupled lattice Boltzmann method and discrete element modelling of particle transport in turbulent fluid flows: computational issues. Int J Numer Meth Eng 72:1111–1134

Flekkoy EG, Malthe-Sorenssen A (2002) Modeling hydrofracture. J Geophys Res B8:2151. doi:10.1029/2000JB000132

Hahn M, Wallmersperger T, Kroplin BH (2010) Discrete element representation of continua: proof of concept and determination of the material parameters. Comput Mater Sci 50:391–402

Hrennikoff A (1941) Solution of problems of elasticity by the framework method. ASME J Appl Mech 8:A619–A715

Hsieh YM, Li HH, Huang TH, Jeng FS (2008) Interpretations on how the macroscopic mechanical behavior of sandstone affected by microscopic properties revealed by bonded-particle model. Eng Geol 99:1–10

Jain AK, Juanes R (2009) Preferential mode of gas invasion in sediments: grain-scale mechanistic model of coupled multiphase fluid flow and sediment mechanics. J Geophys Res 114:B08101–B08119

Kawai T (1978) New discrete models and their application to seismic response analysis of structures. Nucl Eng Des 48(1):207–229

Khoshghalb A, Khalili N, Selvadurai APS (2010) A three-point time discretization technique for parabolic partial differential equations. Int J Numer Anal Meth Geomech 35(3):406–418

Kozicki J, Tejchman J (2008) Modelling of fracture process in concrete using a novel lattice model. Granular Matter 10(5):377–388

Mustoe GGW (1992) Generalized formulation of the discrete element method. Eng Comput 9(2):181–190

Ostoja-Starzewski M (2002) Lattice models in micromechanics. Appl Mech Rev 55(1):35–59

Parisi A, Caldarelli G (2000) Self-affine properties of fractures in brittle materials. Physica A: Stat Mech Appl 280(1):161–165

Potyondy DO, Cundall PA (2004) A bonded-particle model for rock. Int J Rock Mech Min Sci 41(8):1329–1364

Sakaguchi H, Muhlhaus HB (2000) Hybrid modelling of coupled pore fluid-solid deformation problems. Pure Appl Geophys 157:1889–1904

Schiffman RL, Chen ATF, Jordan JC (1969) An analysis of consolidation theories. J Soil Mech Found Div, ASCE 95(SM1):285–312

Terzaghi K, Peck RB (1976) Soil mechanics in engineering practice, 2nd edn. Wiley, New York

Tsuji Y, Kawaguchi T, Tanaka T (1993) Discrete particle simulation of two-dimensional fluidized bed. Powder Tech 77:79–87

Wang G, Al-Ostaz A, Cheng AHD, Mantena PR (2009) Hybrid lattice particle modeling: theoretical considerations for a 2D elastic spring network for dynamic fracture simulations. Comput Mater Sci 44(4):1126–1134

Zhao GF (2010) Development of micro-macro continuum-discontinuum coupled numerical method. PhD thesis, EPFL, Switzerland

Zhao GF, Khalili N (2012) Graphics processing unit based parallelization of the distinct lattice spring model. Comput Geotech 42:109–117

Zhao SF, Zhao GF (2012) Implementation of a high order lattice spring model for elasticity. Int J Solids Struct. doi:10.1016/j.ijsolstr.2012.05.015

Zhao GF, Fang J, Zhao J (2011a) A 3D distinct lattice spring model for elasticity and dynamic failure. Int J Numer Anal Meth Geomech 35:859–885

Zhao GF, Fang JN, Sun L, Zhao J (2011b) Parallelization of the distinct lattice spring model. Int J Numer Anal Meth Geomech. doi:10.1002/nag.1085

Zhao GF, Khalili N, Fang J, Zhao J (2012) A coupled distinct lattice spring model for rock failure under dynamic loads. Comput Geotech 42:1–20